Materials Science and Engineering B 311 (2025) 117781

Contents lists available at ScienceDirect

Materials Science & Engineering B

journal homepage: www.elsevier.com/locate/mseb

Surface topology, bandgap evaluation, and photoluminescence characteristics of Bi_2O_3-B_2O_3-Cr_2O_3: ZrO_2 glass ceramics for visible light devices

Adepu Navalika [a,b], Linganaboina Srinivasa Rao [a,*], Tumu Venkatappa Rao [b,*], Shamima Hussain [c], Sujay Chakravarty [c]

[a] Centre for Nanoscience and Technology, Department of Physics, VNR Vignana Jyothi Institute of Engineering and Technology, Bachupally, Nizampet (S.O), Hyderabad PIN-500090, Telangana, India
[b] Department of Physics, National Institute of Technology, Warangal PIN-506004, Telangana, India
[c] UGC-DAE CSR, Kalpakkam Node, Kokilamedu-603104, Tamilnadu, India

ARTICLE INFO

Keywords:
Glass ceramics
Atomic force microscopy
Absorption spectral fitting
Differential Absorption spectral fitting
Photoluminescence
CIE diagram

ABSTRACT

Bismuth-borate-chromium oxide glass ceramics containing small concentrations of ZrO_2 nanoparticles were synthesized. The AFM images showed uneven grains with crystal stripes of size ≈30-70 nm on surface of the glass ceramic samples. The optical bandgap (E_o) was determined in the range of 2.7 – 3.5 eV, using three different methods viz., Tauc, ASF, and DASF methods. The Tanabe-Sugano diagram has revealed that the Cr^{3+} ions were presented in the strong crystal field with $\frac{D_q}{B} > 2.3$. Photoluminescence spectra have revealed two emission bands by $^2T_{2g}(F) \rightarrow {}^4A_{2g}(F)$ (green emission) and $^2E_g(F) \rightarrow {}^4A_{2g}(G)$ (red emission) transitions of Cr^{3+} ions. The (x, y) coordinates in the CIE diagram were shifted from green to orange region as the concentration of ZrO_2 nanoparticles has increased gradually. These glass ceramics may act as active laser media or LED sources for practical applications in visible band, especially green-yellow-orange band.

1. Introduction

Due to the rapid advancements in optical technologies for solid-state light devices, there has been considerable exploration of tunable laser diodes (LDs) and inorganic light emitting diodes (LEDs) in recent years [1]. Thermally stable devitrified glass ceramics hosting transition metal ions (TMIs) and/or rare earth ions (RIs) can be used as multiphase materials with micro/nano size crystallites dispersed in residual glassy matrices for such applications [2,3]. The optical properties of Cr^{3+} ions in the glass ceramic materials viz., optical bandgap and intensity of luminescence depend on the host lattice structure in presence of crystal field by the surrounding ligands. Hence, the glass ceramics doped with active chromium ions (Cr^{3+} ions) can perform as promising luminescent materials in visible and NIR region [2,4]. The Cr^{3+} ion interacts very well with the crystal field and it acts as a luminescent activator. The Cr^{3+} ions activated host materials such as glasses [5], glass ceramics [6], crystals [7], and phosphors [8] exhibit absorption bands in the range of UV to red in visible spectrum. Consequently, the Cr^{3+} ions- doped hosts have been investigated for promising applications in broadband NIR fluorescent devices [5], solid-state lighting [6], fluorescent thermometers [7,8], high power LEDs [7,8], visible LDs [7], and other practical sensors [7,8].

Glass ceramic materials are inorganic solid compounds often fabricated by heat treatment of glasses. The glass ceramics are composed of nano-crystals and/or micro-crystals grown through well controllable crystallization process in glass matrix. The ductile nature of amorphous glass matrix, combined with the mechanical strength of the crystalline phase makes glass ceramics as exceptional technological materials. They offer the advantages of customary glasses and ceramics, demonstrating excellent mechanical as well as optical properties for practical applications [2,3,6]. B_2O_3 (boron trioxide) is widely used as classical vitreous glass product due to its strong covalent B-O bonds. B_2O_3 has high coordination numbers (3&4), which helps in the formation of high stable glass network by means of BO_3 and BO_4 units along with B-O-B, O-B-O chains [9–12]. Usually, in most of the cases, Bi_2O_3 acts as glass network modifier with BiO_6 units in presence of some transition metal oxides

* Corresponding authors.
E-mail addresses: srinivasarao_l@vnrvjiet.in, lsr9@rediffmail.com (L. Srinivasa Rao), tvraokmm@nitw.ac.in (T. Venkatappa Rao).

https://doi.org/10.1016/j.mseb.2024.117781
Received 4 September 2024; Received in revised form 19 October 2024; Accepted 24 October 2024
Available online 1 November 2024

(like Cr_2O_3) [9–12]. Bi_2O_3-B_2O_3 glass ceramics co-doped with Cr_2O_3 and ZnO/ZrO_2 are well known for their technological importance owing to their inventive thermal, micro-structural, structural, magnetic, optical, and radiation shielding properties. These glass ceramics are expedient of easy manufacturing, low cost, homogeneous doping of nanoparticles, and good optical transparency over UV–Visible-NIR region [9–12].

Usually, boron ions exist in [BO_3] and [BO_4] units in the bismuth borate glass ceramic structure. The [BO_4] tetrahedron associates with cations like Bi^{3+}, Cr^{3+}, Zn^{2+}, and Zr^{4+} ions, and reinforces the stable glass ceramic network with [BiO_3], [CrO_4], [ZnO_4], and [ZrO_4] units respectively [9–12]. The morphology and respective phase transformation of the glass ceramics can be influenced by the content of nucleating agents (like Cr_2O_3 and ZrO_2 nanoparticles) and the process of heat treatment as reported in our earlier work [11,12]. Moreover, both modifying reaction of stable trivalent Bi^{3+} ions of Bi_2O_3 and tetravalent Zr^{4+} ions of ZrO_2 can create defects in the borate glass ceramic system, influencing the photoluminescence properties of Cr^{3+} ions. In this paper, we would like to explore the optical absorption and photoluminescence characteristics of the Bi_2O_3-B_2O_3-Cr_2O_3: ZrO_2 glass ceramics coupled with their surface characteristics.

Atomic force microscopy (AFM) is a powerful technique used for imaging and characterizing the surfaces of the materials at the level of nanoscale. The displacement control is in the order of ≈0.01 nm, and the sample tip contact area is about ≈10 nm typically. AFM can be used to study the surface topology of a wide range of materials, including glass ceramics [13]. The AFM of these glass ceramics allows us for visualization and measurement of their surface roughness, texture, waviness, and topological features with high accuracy [13,14]. F. Abdi [15] reported influence of porosity and particle size (grain size) on optical absorption, transmittance, and dielectric properties of the manganese thin films. F. Juhim et al. [16] studied of gamma irradiation behavior of TiO_2 and Al_2O_3 nanoparticles doped- tellurite glasses in terms of average surface roughness (R_a) and root mean square roughness (R_q) obtained by AFM. Zhichao Lou & team [17] reviewed physical, chemical, mechanical, and structural properties of biomass materials such as cellulose, wood, and bamboo in the light of AFM studies. L. Auvray et al. [18] investigated a defect related wide NIR photoluminescence band (≈1040 nm) of GaAsN epoxy, associating it with its morphology (surface roughness, R_q) attained by AFM. However, there are no adequate number of studies on correlation between AFM surface imaging and both absorption & emission phenomena of glass ceramics in the literature. Thus, the objective of this paper is to extract topological surface parameters of Bi_2O_3-B_2O_3-Cr_2O_3: ZrO_2 glass ceramics by AFM, consequently to study their optical properties (especially, absorption and photoluminescence) for potential applications [2,16,19,20].

2. Materials and methods

2.1. Composition of glass ceramics

The chemical compositions (in mol %) were chosen as follows: $30Bi_2O_3$-$70B_2O_3$ (pure) and (29-x)Bi_2O_3-$70B_2O_3$-$1Cr_2O_3$:xZrO_2 ($0 \leq x \leq 2$). Bismuth-borate-chromium oxide glass ceramics hosting ZrO_2 nanoparticles were synthesized by two-step heat treatment (step-1: nucleation and step-2: crystallization) as reported in our earlier work [11,12]. The parent glass samples were synthesized by a series of thermal processes: first, the chemical compositions were melted at ≈1200 °C for 1 h in a muffle furnace, then quickly quenched on a preheated brass plate at 100 °C, and finally annealed at 350 °C for 1 h in an annealing chamber. Next, these parent glass samples were nucleated at 400 °C for 4hrs (first step heat treatment) and then processed crystal growth at 550 °C for 1 h (second step heat treatment), resulting in glass ceramic samples. The samples were designated as: BBC_0Zr_0 (pure), BBC_1Zr_0 (for x = 0 mol %), $BBC_1Zr_{0.5}$ (for x = 0.5 mol %), BBC_1Zr_1 (for x = 1 mol %), $BBC_1Zr_{1.5}$ (for x = 1.5 mol %), and BBC_1Zr_2 (for x = 2 mol %).

2.2. Surface topology by AFM

The AFM topographic images of the samples were recorded with a resolution of 512 X 512 pixels with the aid of semi-contact (tapping) mode of the atomic force microscope (*model: NT-MDT's NTEGRA AURA*) at a resonant frequency of 243 kHz and stiffness constant of 11 N/m. The microscope was operated with a probe containing a rectangular shaped silicon tip of width 35 nm and thickness 3 nm. Applying open-source software tool known as '*Gwyddion*' [21] to the recorded AFM images, the surface morphological characteristics viz., average roughness (R_a), rms roughness (R_q), surface skewness (R_{sk}), Kurtosis coefficient (R_{ku}), etc. have been determined using the following equations [14,22]:

i) The average roughness, $$R_a = \frac{1}{N_x N_y}\sum_{i=1}^{N_x}\sum_{j=1}^{N_y}\left|Z_{(i,j)} - Z_{mean}\right| \quad (1)$$

where, $$Z_{mean} = \frac{1}{N_x N_y}\sum_{i=1}^{N_x}\sum_{j=1}^{N_y} Z_{(i,j)} \quad (2)$$

ii) Root mean square (RMS) roughness, R_q

$$= \sqrt{\frac{1}{N_x N_y}\sum_{i=1}^{N_x}\sum_{j=1}^{N_y}\left(Z_{(i,j)} - Z_{mean}\right)^2} \quad (3)$$

iii) Surface skewness, $$R_{sk} = \frac{\frac{1}{N_x N_y}\sum_{i=1}^{N_x}\sum_{j=1}^{N_y}\left(Z_{(i,j)} - Z_{mean}\right)^3}{R_q^3} \quad (4)$$

iv) Kurtosis coefficient, $$R_{ku} = \frac{\frac{1}{N_x N_y}\sum_{i=1}^{N_x}\sum_{j=1}^{N_y}\left(Z_{(i,j)} - Z_{mean}\right)^4}{R_q^4} - 3 \quad (5)$$

where, Z_{mean} is mean height of all points in the selected area of the AFM image, $Z_{(i,\ j)}$ is height at corresponding i & j points, N_x and N_y are respective number of points along the x-axis and y-axis of the recorded AFM image.

2.3. Evaluation of optical bandgap (E_o) and Urbach energy (E_u)

Jasco UV–Visible spectrophotometer (*model: V-750*) was operated to monitor the optical absorption spectra of the highly polished samples. Absorption edge ($\lambda_{cut\text{-}off}$) and absorption coefficient ($\alpha(\nu)$) were determined experimentally. Thus, the optical bandgap (E_o) of the glass ceramics were determined by three methods such as i) Tauc method, ii) Absorption spectral fitting (ASF), and iii) Differential absorption spectral fitting (DASF).

2.3.1. Tauc method

The optical bandgap (E_o) was determined by Tauc plots using the relation [23]:

$$\alpha(\upsilon)h\upsilon = C(h\upsilon - E_o)^m \quad (6)$$

where, E_o is optical bandgap, $h\upsilon$ is photon energy, C is a proportional constant, and m is another constant, which explains type of transition. The value of m is considered as 2 for indirect allowed transitions for the present glass ceramics. This method takes account of the absorption coefficient ($\alpha(\upsilon)$) of the sample (in turn, thickness of the sample (d)) and type of the transition (value of m). The Urbach energy (E_u) of the BBCZr glass ceramics is evaluated using Urbach rule in terms of slope of linear relationship between $ln\alpha(\upsilon)$ and $h\upsilon$ as follows [24]:

$$\alpha(\upsilon) = \alpha_o e^{\frac{h\upsilon}{E_u}} \quad (7)$$

$$ln[\alpha(\upsilon)] = \frac{h\upsilon}{E_u} + ln[\alpha_o] \quad (8)$$

$$E_u = \frac{1}{slope} \tag{9}$$

2.3.2. ASF method

The optical bandgap was determined by ASF method suggested by D Souri et al. using the relation [25]:

$$E_o = \frac{hc}{\lambda_g} \tag{10}$$

where, λ_g is threshold wavelength, which can be obtained from the plot of $(\frac{A}{\lambda})^2$ versus $\frac{1}{\lambda}$ by the relation:

$$A(\lambda) = D\lambda\left(\frac{1}{\lambda} - \frac{1}{\lambda_g}\right)^m \tag{11}$$

where, A is absorbance of the sample, λ is wavelength of incident light, and $D = (hc)^{m-1} * \frac{d}{2.303}$ (here, d is sample thickness).

The Urbach energy (E_u) of the BBCZr glass ceramics is evaluated using Urbach rule in terms of slope of linear relationship between ln*[A (λ)]* and $\frac{1}{\lambda}$ as follows [25]:

$$A(\lambda) = A_o e^{\frac{hc}{E_u}\left(\frac{1}{\lambda}\right)} \tag{12}$$

$$ln[A(\lambda)] = \frac{hc}{E_u}\left(\frac{1}{\lambda}\right) + ln[A_o] \tag{13}$$

$$E_u = \frac{hc}{slope} \tag{14}$$

2.3.3. DASF method

D Souri et al. proposed DASF method to compute the optical bandgap (E_o) by using the Eq. (10) in terms of threshold wavelength (λ_g) with the help of differential form of Eq. (11) as follows [26]:

$$\frac{d\left\{ln\left[\frac{A(\lambda)}{\lambda}\right]\right\}}{d\left(\frac{1}{\lambda}\right)} = \frac{m}{\left(\frac{1}{\lambda} - \frac{1}{\lambda_g}\right)} \tag{15}$$

Also, D Souri et al. proposed DASF method to determine the Urbach energy ($E_u = \frac{hc}{slope}$) in terms of slope of linear relation between $ln\left[\frac{A(\lambda)}{\lambda}\right]$ versus $\left(\frac{1}{\lambda}\right)$ by rearranging Eq. (12) as follows [26]:

$$ln\left[\frac{A(\lambda)}{\lambda}\right] = \frac{hc}{E_u}\left(\frac{1}{\lambda}\right) + ln\left[\frac{A_o}{\lambda}\right] \tag{16}$$

In this way, three methods i.e, Tauc method, ASF, and DASF methods have been used to obtain the optical bandgap (E_o) and Urbach energy (E_u) of the BBCZr glass ceramics from their experimental optical absorption spectra.

2.4. Excitation and emission

First, the excitation spectra of the BBCZr samples have been captured using xenon lamp as the excitation source, choosing an expected emission band in red region (≈694 nm) as reported in the literature [27,28]. Thus, the excitation wavelength was determined as ≈421 nm, corresponding to a prominent peak in the spectra for all the samples. Later, the emission spectra have been recorded by exciting the samples at the predetermined value of excitation wavelength (≈421 nm). The excitation spectra (for $\lambda_{emission}$ = 694 nm) and photoluminescence spectra (at $\lambda_{excitation}$ = 421 nm) of the samples were monitored by Jobin Yvon (*model: Fluorolog-321*) at room temperature [29].

3. Results and Discussion

3.1. Atomic force microscopy

Fig. 1 shows the AFM topographic images of the BBCZr glass ceramics. Insets (a) and (b) of the Fig. 1 show the 3D view and cross-sectional profile of one sample (BBC_1Zr_2 glass ceramic) drawn using *Gwyddion* software [21]. The AFM morphographs displayed the uneven grains on the surface and different sized rocky and wrinkled *meso*-porous structures of the prepared glass ceramics. The roughness on the surface of the samples may be attributed to the heterogeneous crystallization, voids, pores, surface defects, etc. In view of the AFM images, vertical growth of crystal stripes of size around 30 nm to 70 nm can be observed in all the heat-treated glasses. Thus, we can confirm that these BBCZr glass ceramic samples exhibit both amorphous and crystalline nature after the heat treatment [11,12]. Y. Zhang et al. [13] have reported the size of heterogeneous crystalline phase up to 100 nm around the homogeneous amorphous phase of the heat treated silica glass ceramics. The surface roughness parameters (shown in Table 1) have been determined using *Gwyddion* software [21].

3.1.1. Average roughness (R_a) and rms roughness (R_q)

The parameters average roughness (R_a) and rms roughness (R_q) provide the mean absolute value of surface roughness over the scan area and degree of variation in surface roughness of the samples respectively [22,30,31]. The values of R_a of the samples are observed in the range of 7.714–10.763 nm and their average value of 8.903 nm. The values of R_q of the samples are observed in the range of 9.991–15.426 nm and their average value of 12.136 nm. The sample BBC_1Zr_1 has shown the highest values of R_a and R_q, indicating its surface is rougher than other samples [22,30]. Consequently, this sample exhibits the maximum crystal growth with larger grain size after the heat-treatment. On the other hand, the sample BBC_0Zr_0 has obtained the minimum values of R_a and R_q, showing the lowest roughness among the studied samples [31]. As a result, this sample shows the lowest affinity for crystal growth exhibiting less number of grains with small size. The reason behind this may be the absence of nucleating agents namely, Cr_2O_3 and ZrO_2 nanoparticles in the composition of the pure sample (BBC_0Zr_0).

3.1.2. Surface skewness (R_{sk}) and Kurtosis coefficient (R_{ku})

The surface skewness (R_{sk}) is the symmetry of height distribution due to the crystal growth under the analyzed surface of the sample. The R_{sk} value is negative for BBCZr samples, demonstrating the presence of more number of peaks than troughs [22]. This observation suggests that these samples have good tendency of crystal growth after the heat treatment [11,12,13]. In view of the cross-sectional profiles of AFM images as shown in Fig. 1, the sample BBC_1Zr_1 has the highest surface skewness among the series of the samples. The Kurtosis coefficient (R_{ku}) is a very distinctive parameter that illustrates the concentration of peak height distribution at the mean value on the scanned surface area. The surface height distribution can be identified as follows: i) normal distribution for $R_{ku} = 0$, ii) highly concentrated near the average value for $R_{ku} > 0$, and iii) dispersed distribution for $R_{ku} < 0$ [22]. The values of R_{ku} have been obtained in the range of 1.526–6.232 with the average 3.540. Thus, all the crystallized surfaces have exhibited $R_{ku} > 0$, indicating presence of highly concentrated sharp peaks around the mean value [22,32].

3.2. Optical absorption spectroscopy

3.2.1. Cut-off wavelength ($\lambda_{cut\text{-}off}$) and absorption bands

Fig. 2 shows the absorption spectra of BBCZr glass ceramics. The pertinent data is shown in Table 2. The spectra have shown the bands attributed to the co-existence of chromium ions in the form of Cr^{3+}, Cr^{5+}, and Cr^{6+} ionic states in the samples [9,33,34]. The absorption edge is detected at 319 nm for the pure sample (BBC_0Zr_0). It shifts towards longer wavelengths up to x = 1 mol %, and then it shifts towards

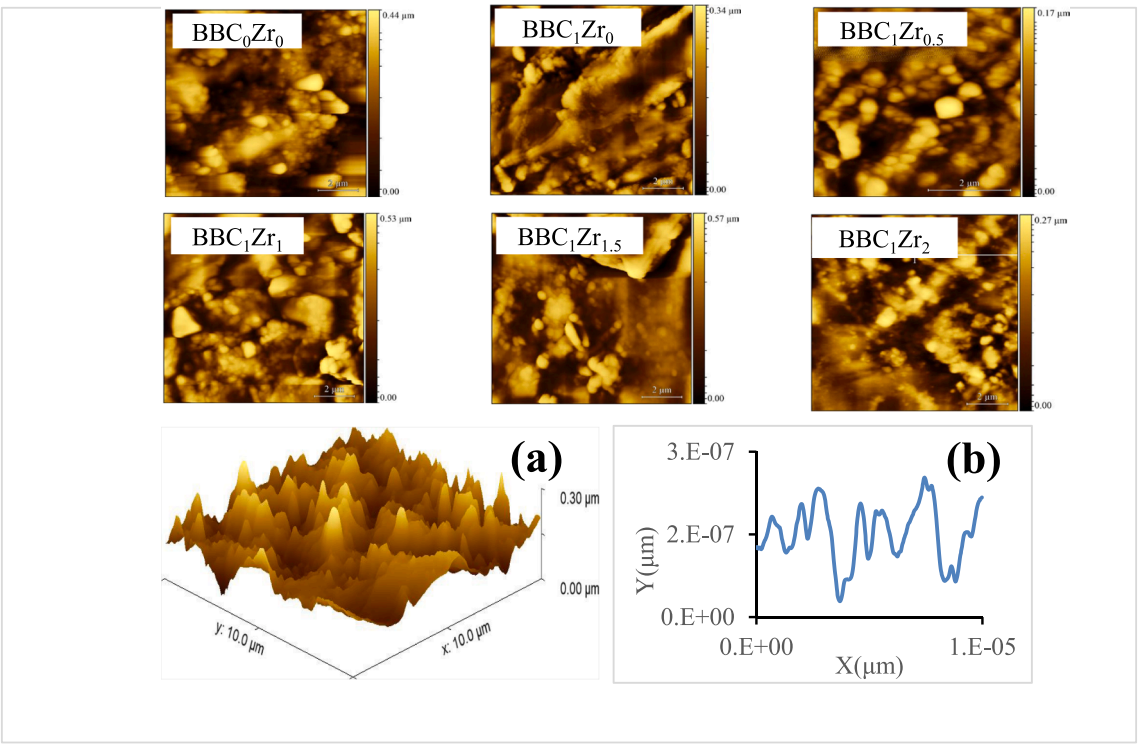

Fig. 1. AFM images of BBCZr glass ceramics. Inset (a) 3D view and (b) Cross-sectional profile of BBC_1Zr_2 glass ceramic.

Table 1
Topological profile parameters of BBCZr glass ceramics.

Sample	Average roughness (R_a) nm	RMS roughness (R_q) nm	Surface skewness (R_{sk})	Kurtosis coefficient (R_{ku})
BBC_0Zr_0	7.714	9.991	−0.139	1.526
BBC_1Zr_0	7.850	10.360	−0.193	2.252
$BBC_1Zr_{0.5}$	8.246	10.993	−0.205	2.667
BBC_1Zr_1	10.763	15.426	−0.553	6.232
$BBC_1Zr_{1.5}$	9.909	14.021	−0.473	5.522
BBC_1Zr_2	8.941	12.024	−0.370	3.042
Average value	8.904	12.136	−0.322	3.540

shorter wavelengths for x > 1 mol % of ZrO_2 nanoparticles in the glass ceramics.

The BBCZr glass ceramics have revealed four optical absorption bands through the d-d transitions such as $^4A_{2g}(F)$ to $^4T_{1g}(F)$, $^4T_{2g}(F)$, $^2T_{1g}(G)$, and $^2E_g(G)$ due to presence of Cr^{3+} ions in octahedral symmetry in the range of ≈440-445 nm, ≈614-625 nm, ≈649-655 nm, and ≈715-721 nm respectively [9,33,34]. It is well known that Cr^{6+} ion has [Ar] $3d^0$ configuration. The ground state ($3d^02p^6$) of Cr^{6+} ion transforms into excited state ($3d^12p^5$) of Cr^{5+} ion through charge transfer transition. The Cr^{6+} ions can be existed as $Cr^{6+}O^{2-}$ sites with $[CrO_4]^{2-}$ units, whereas the Cr^{5+} ions may be presented as $Cr^{5+}O^{-}$ sites with $[CrO_4]^{3-}$ units as follows [27,33,35]: $Cr^{6+}\left(3d^02p^6\right)\rightarrow Cr^{5+}\left(3d^12p^5\right)(t_1^5,2e)$ and $Cr^{6+}\left(3d^02p^6\right)\rightarrow Cr^{5+}\left(3d^12p^5\right)(t_1^5,4t_2)$. These two charge transfer transitions are noticed in the ranges of ≈344-356 nm and ≈360-365 nm respectively [33,34]. As well, we may expect a charge transfer transitions of Bi^{3+} ions along with the Cr^{6+} ions in UV region ≈344-356 nm [9,36,37,38]. Also, a clear blue band is observed in the range of ≈457-464 attributed to the excitation of Cr^{5+} ions in the form of $[CrO_4]^{3-}$ units [33]. These transitions may modify the boron coordination $[BO_3] \leftrightarrow [BO_4]$ units and zirconium coordination $[ZrO_6] \leftrightarrow [ZrO_4]$ units by means of simultaneous change of chromium coordination $[CrO_4]^{2-} \leftrightarrow [CrO_4]^{3-} \leftrightarrow [CrO_6]$ units and bismuth coordination $[BiO_6] \leftrightarrow [BiO_3]$ units in the glass ceramic matrix as reported in our earlier FTIR and Raman spectroscopic studies [11,12].

An illustration of intrinsic glass ceramic structure of the sample BBC_1Zr_2 is presented in Fig. 3, using Avogadro chemical editor [39]. The host glass ceramic system has exhibited interaction of various functional groups $[BiO_3]$, $[BiO_6]$, $[BO_4]$, $[BO_3]$, $[ZrO_4]$, and $[ZrO_6]$ units. The figure clearly depicts the framework of chromium ions in three stable ionic states Cr^{6+}, Cr^{5+}, and Cr^{3+} states connected with $[CrO_4]^{2-}$, $[CrO_4]^{3-}$, and $[CrO_6]$ structural units respectively. When Cr_2O_3 and ZrO_2 are co-doped into the composition, the Cr^{3+} ions (of small ionic radius ≈0.755 A°) are expected to replace Zr^{4+} ions (of larger ionic radius ≈0.86 A°) in the ZrO_6 octahedral positions generating oxygen vacancies (V_o). The possible Krozer-Vink notation for such oxygen vacancies is as follows [40]: $2Zr_{Zr}^{4+} + 4O_o^{2-} \xrightarrow{Cr^{3+}\ substitution} 2Cr_{Zr}^{3+} + 3O_o^{2-} + V_o^{\cdot\cdot} + 2e' + \frac{1}{2}O_2\uparrow$. The oxygen vacancies (defects) created during the preparation of the glass ceramics can generate localized states of free electron charges within the bandgap, affecting their optical absorption characteristics. In Cr_2O_3- doped glass ceramics, these defects may interact with Cr^{6+}, Cr^{5+}, and Cr^{3+} ions, leading to specific absorption bands (especially at shorter wavelengths as observed in the range of ≈350 – 450 nm) associated with electronic transitions among these states by means of charge transfer mechanism [33,34].

3.2.2. Optical bandgap (E_o) and Urbach energy (E_u) by Tauc, ASF, and DASF methods

The optical bandgap (E_o) for indirect allowed transitions ($m = 2$) have been determined by three methods such as i) Tauc method, ii) ASF method, and iii) DASF method as shown in Fig. 4, Fig. 5, and Fig. 6 respectively. The insets of Fig. 4, Fig. 5, and Fig. 6 show the calculation of Urbach energy (E_u) in these three methods i) Tauc method, ii) ASF method, and iii) DASF methods respectively. The values of E_o and E_u obtained from these three methods are recorded in Table 3.

These three methods are distinct each other by the way of procedure to obtain the optical bandgap (E_o) and Urbach energy (E_u) of the BBCZr glass ceramics. The Tauc method mostly depends on absorption coefficient ($\alpha(\upsilon)$) and thickness (d) of the BBCZr glass ceramic samples. There

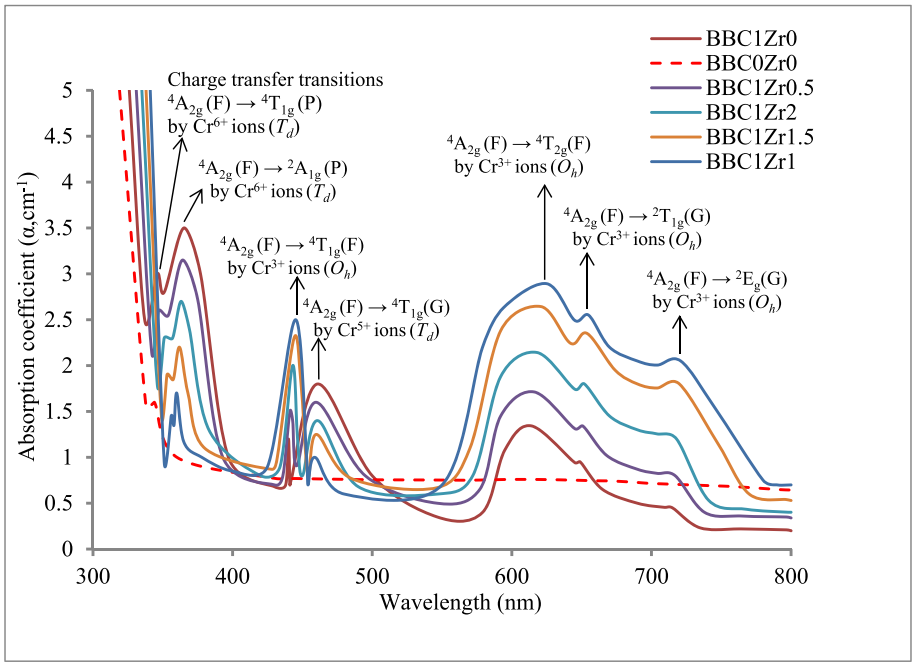

Fig. 2. Optical absorption spectra of BBCZr glass ceramics.

Table 2
Summary of the data on optical absorption spectra of BBCZr glass ceramics.

Sample	Cut-off wavelength ($\lambda_{cut\text{-}off}$) nm	Charge transfer transitions of Cr^{6+} ions in tetrahedral form (T_d) of $[CrO_4]^{2-}$ units		Transitions of Cr^{5+} ions in tetrahedral form (T_d) of $[CrO_4]^{3-}$ units	Transitions of Cr^{3+} ions in octahedral form (O_h) of $[CrO_6]$ units			
		$^4A_{2g}(F) \rightarrow {}^4T_{1g}(P)$	$^4A_{2g}(F) \rightarrow {}^2A_{1g}(P)$	$^4A_{2g}(F) \rightarrow {}^4T_{1g}(G)$	$^4A_{2g}(F) \rightarrow {}^4T_{1g}(F)$	$^4A_{2g}(F) \rightarrow {}^4T_{2g}(F)$	$^4A_{2g}(F) \rightarrow {}^2T_{1g}(G)$	$^4A_{2g}(F) \rightarrow {}^2E_g(G)$
BBC_0Zr_0	319	344	–	–	–	–	–	–
BBC_1Zr_0	326	346	365	461	440	614	649	715
$BBC_1Zr_{0.5}$	331	347	364	460	441	616	651	717
BBC_1Zr_1	341	356	360	459	445	625	655	721
$BBC_1Zr_{1.5}$	338	353	362	460	444	621	654	720
BBC_1Zr_2	335	351	363	461	443	618	652	718

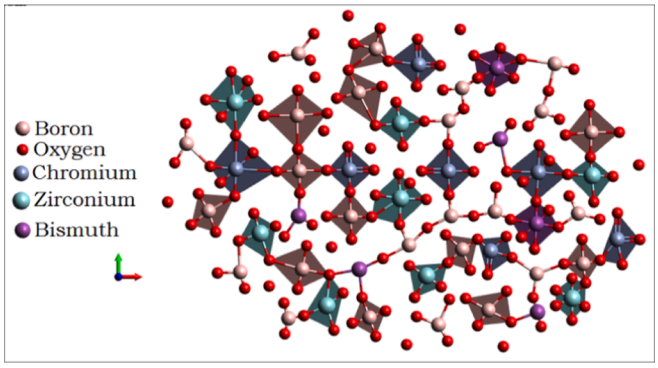

Fig. 3. An illustration of intrinsic glass ceramic structure of the sample BBC_1Zr_2.

may be fractional deviation in the measured values of E_o and E_u. Because the thickness of the samples (d) may not be uniform and also it is not easy to measure the thickness (d) precisely in all cases. On the other hand, the ASF and DASF methods do not take thickness of samples in account; thereby they increase accuracy of the measurement of E_o and E_u [25,26]. In Tauc and ASF methods, the value of m can be chosen by the best fit of linear relation by the least squares method. Whereas, the DASF method determines E_o and E_u without any assumption of type of transition (in terms of m). The DASF method is useful to define type of transition by evaluating m, which is nothing but the slope of linear relation between $ln\left[\frac{A(\lambda)}{\lambda}\right]$ versus $ln\left(\frac{1}{\lambda}-\frac{1}{\lambda_g}\right)$ (as shown in Fig. 7) by rearranging the Eq. (11) as follows [26]:

$$ln\left[\frac{A(\lambda)}{\lambda}\right] = mln\left(\frac{1}{\lambda}-\frac{1}{\lambda_g}\right) + ln[D] \tag{17}$$

Fig. 7 confirms the nature of the transition as indirect allowed transition by providing its slope $= m \approx 2$ in the linear region, which is acceptable for the semiconductor glass ceramics [38].

The values of Urbach energy (E_u) of the samples obtained from the three methods are constituent [41]. However, the values of optical bandgap (E_o) of the samples (except pure sample) obtained from DASF method is smaller (≈0.7 eV) than that of the values obtained from both Tauc method and ASF method. This may be occurred due to the occupation of free charges into the bandgap through the significant charge transfer transitions (≈0.7 eV) of chromium ions (Cr^{6+} and Cr^{5+} ions) below the actual absorption edge [35]. The values of E_o obtained from DASF method are more accurate, because this method does not include the effect of charge transfer transitions in the UV region. Thus, the DASF method is more advantageous than the remaining two methods.

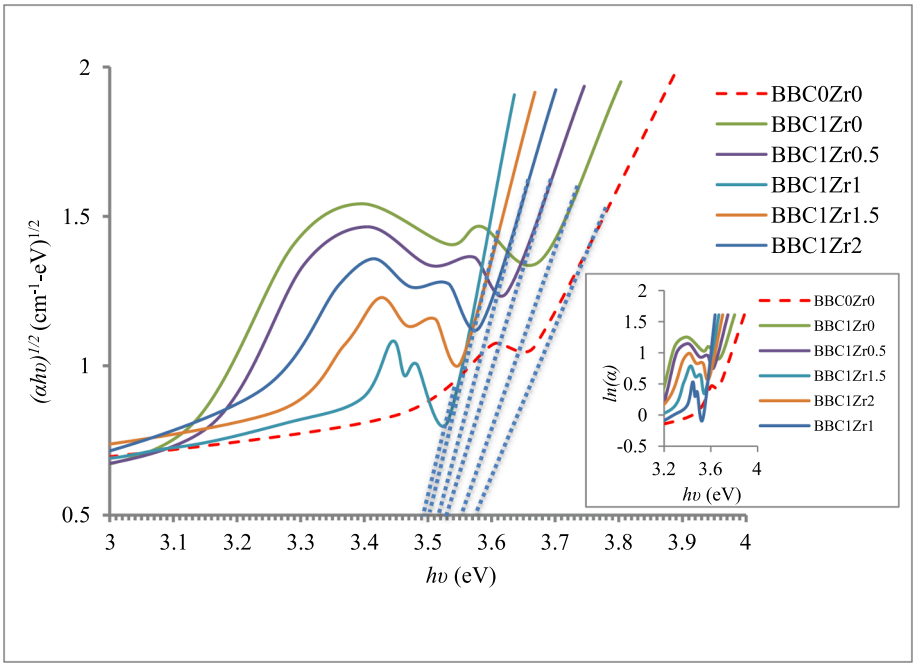

Fig. 4. Tauc plots of BBCZr glass ceramics for indirect allowed transitions. Inset: Calculation of Urbach energy by ln(α) versus ($h\nu$) plots.

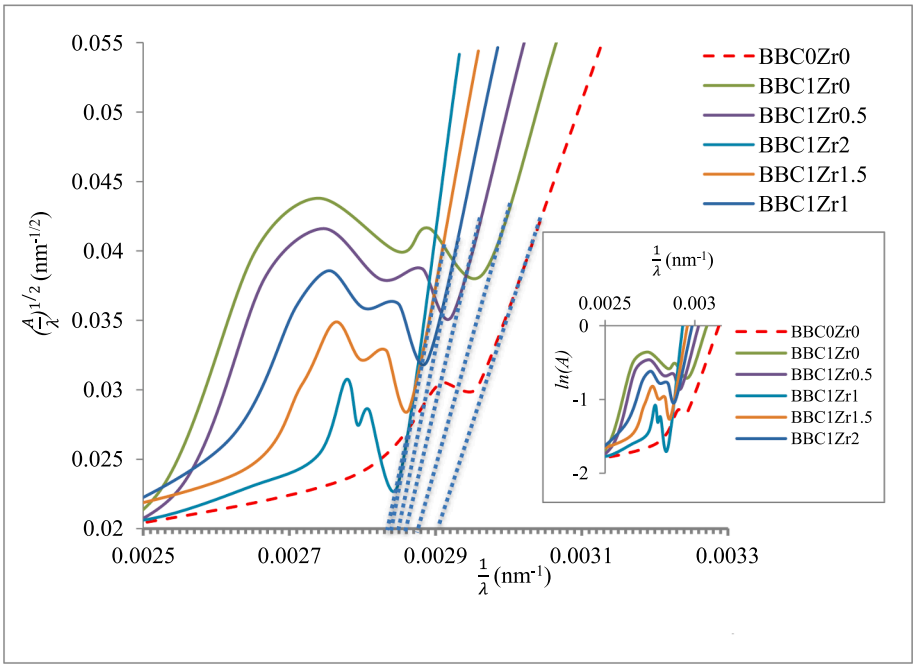

Fig. 5. Absorption spectrum fitting (ASF) plots of BBCZr glass ceramics for indirect allowed transitions. Inset: Calculation of Urbach energy by ln(A) versus ($\frac{1}{\lambda}$) plots.

3.2.3. *Anderson localization and Moss-Burstein effect*

The optical bandgap (E_o) of the BBCZr samples is decreased up to x = 1 mol % of ZrO_2. Since, there is a gradual redshift in the absorption edge with increased intensity of absorption bands of Cr^{3+} ions, owing to creation of more number of non-bridging oxygens (NBOs) and charge (free electron) defects [38]. The Zr^{4+} ions can create large number of density of states of electrons around the Cr^{3+} ions with the [CrO_6] octahedral sites in the glass ceramic; consequently, the excited electrons can be overlapped with the empty 3d- states of the nearest [CrO_6] sites [9,38]. Therefore, the impurity band of defects emerges into the actual bandgap. Hence, the absorption edge and absorption bands of Cr^{3+} ions (in octahedral form) exhibit redshift as observed, which is responsible for reduction in the optical bandgap (E_o) of the BBCZr samples containing up to x = 1 mol % of ZrO_2 nanoparticles in the composition by means of '*Anderson localization*' of charges in amorphous solids [38,42,43].

The bandgap (E_o) has been increased for x > 1 mol% of ZrO_2. And, the intensity of absorption bands Cr^{6+} and Cr^{5+} ions (in tetrahedral form) increases at the cost of intensity of Cr^{3+} ions (in octahedral form) as displayed in Fig. 2. Then the free charges and NBOs of donor levels can be surrounded by Cr^{6+} and Cr^{5+} ions and increase network forming sites of $[CrO_4]^{2-}$ and $[CrO_4]^{3-}$ units respectively. Therefore, the amount of free charges and NBOs can be decreased. Thus, the impurity band can be squeezed considerably at the vacant 3d- states of nearby chromium

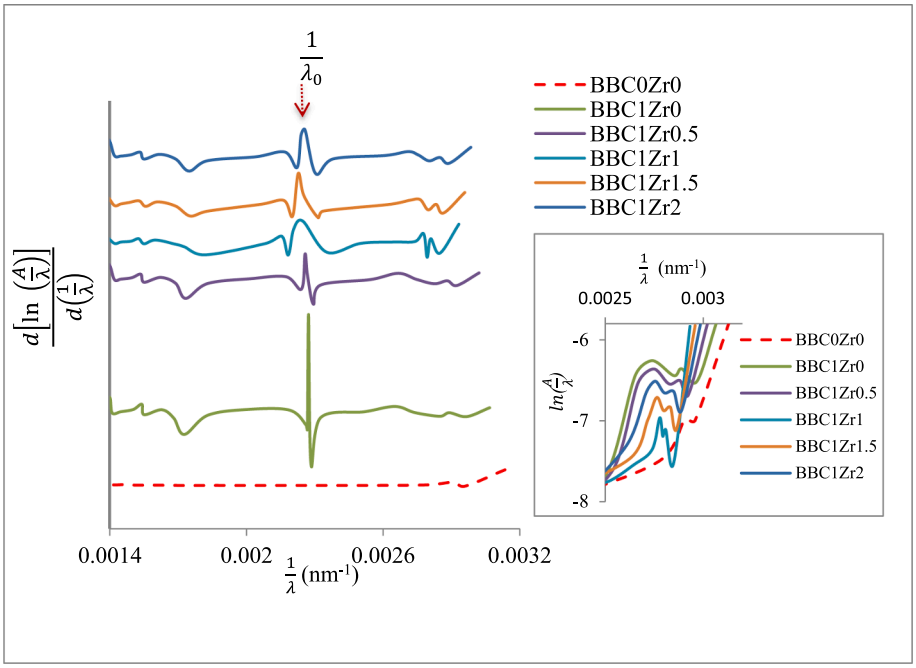

Fig. 6. Differential absorption spectrum fitting (DASF) plots of BBCZr glass ceramics Inset: Calculation of Urbach energy by $ln(\frac{A}{\lambda})$ versus $(\frac{1}{\lambda})$ plots.

Table 3
The optical bandgap (E_o) and Urbach energy (E_u) of BBCZr glass ceramics.

Sample	Tauc method		ASF method		DASF method	
	E_o (eV)	E_u (eV)	E_o (eV)	E_u (eV)	E_o (eV)	E_u (eV)
BBC_0Zr_0	3.572	0.187	3.608	0.188	3.604	0.177
BBC_1Zr_0	3.551	0.179	3.583	0.180	2.818	0.171
$BBC_1Zr_{0.5}$	3.534	0.143	3.565	0.144	2.799	0.138
BBC_1Zr_1	3.491	0.094	3.521	0.098	2.786	0.069
$BBC_1Zr_{1.5}$	3.505	0.110	3.534	0.112	2.792	0.094
BBC_1Zr_2	3.513	0.115	3.546	0.115	2.799	0.112

ions. Hence, the absorption edge and absorption bands of Cr^{3+} ions (in octahedral form) exhibit blueshift, and bandgap enhances for x > 1 mol % of ZrO_2 in the BBCZr glass ceramics by means of '*Moss-Burstein effect*' [38,44].

3.2.4. *Tanabe-Sugano diagram*

The optical absorption characteristics of Cr^{3+} ions in the BBCZr glass ceramic hosts have been explored (as shown in Table 4) in terms of crystal field parameter (D_q), Racah parameters (B & C), and Nephelauxetic parameter (h) [45,46] with the help of peak points of three prominent energy bands observed in spectra such as E_1: $^4A_{2g}(F) \rightarrow {}^4T_{2g}(F)$, E_2: $^4A_{2g}(F) \rightarrow {}^4T_{1g}(F)$, and E_3: $^4A_{2g}(F) \rightarrow {}^2E_g(G)$ in cm^{-1}. The

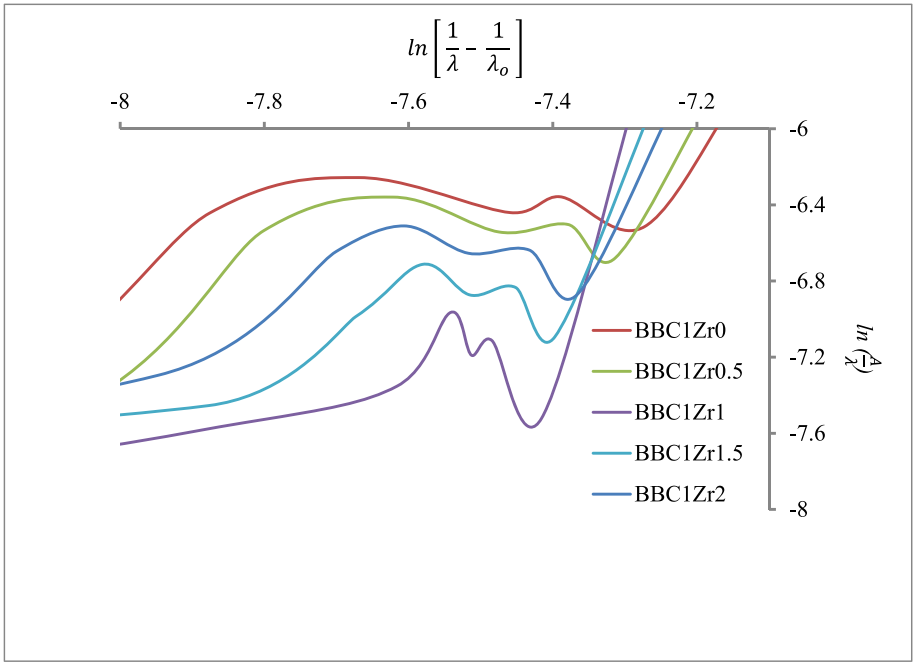

Fig. 7. Calculation of type of transition (m value) of BBCZr glass ceramics by $ln\left[\frac{1}{\lambda}-\frac{1}{\lambda_o}\right]$ versus $\ln(\frac{A}{\lambda})$ plots.

Table 4
Crystal field parameter (D_q), Racah parameters (B & C), Nephelauxetic ratio (β) and Nephelauxetic parameter (h) of Cr^{3+} ions in BBCZr glass ceramic hosts.

Sample	D_q cm^{-1}	B cm^{-1}	$\frac{D_q}{B}$	C cm^{-1}	β	h
BBC_1Zr_0	1628.664	641.651	2.538	3072.788	0.699	1.434
$BBC_1Zr_{0.5}$	1623.377	642.506	2.527	3058.666	0.700	1.429
BBC_1Zr_1	1600.000	649.643	2.463	3020.406	0.708	1.392
$BBC_1Zr_{1.5}$	1610.306	641.226	2.511	3043.545	0.699	1.436
BBC_1Zr_2	1618.123	636.601	2.542	3065.326	0.693	1.460

parameter D_q is obtained from the energy (E_1):

$$D_q = \frac{E_1}{10} \tag{18}$$

The parameter B is calculated in terms of E_1 and E_2 using the relations [47,48]:

$$\frac{D_q}{B} = \frac{15(x-8)}{x^2-10x} \tag{19}$$

where,

$$x = \frac{E_2 - E_1}{D_q} \tag{20}$$

Inter-electronic repulsion parameter B_{free} of Cr^{3+} free ion has been reported as 918 cm^{-1} in the literature [49]. Now, the observed value of B is found to be in the range of 637–649 cm^{-1}. Hence, the Nephelauxetic ratio ($\beta = \frac{B}{B_{free}}$) of the samples is computed as shown in Table 4. The value of β is higher for the sample BBC_1Zr_1, and it may be attributed to the maximum effect of Coulomb repulsive forces among the 3d- electrons of Cr^{3+} ions, which reduces the covalent nature of Cr^{3+} ions in presence of the strong crystal field in the form of [CrO_6] octahedral units [33]. The parameter C can be determined with the help of known values of E_3, D_q, and B using the following expression [50]:

$$\frac{C}{B} = \frac{1}{3.05}\left(\frac{E_3}{B} - 7.9 + 1.8\left(\frac{B}{D_q}\right)\right) \tag{21}$$

Using these equations, the obtained values of B and C for these samples is approximated as $\frac{C}{B} \approx 4.649 - 4.819$ as reported in the literature [51,52]. Thus, these samples can be used as Cr^{3+} activated phosphors for the practical applications [52]. The nature of Cr-O bonding of [CrO_6] octahedron can be identified by Nephelauxetic parameter h, using the following relation [52]:

$$h = \frac{\left[\frac{B_{free} - B}{B_{free}}\right]}{k_{cr^{3+}}} \tag{22}$$

The value of h is estimated as ≈1.4 for the present samples (as shown in Table 4), and the value of k for Cr^{3+} ion is assumed to be ≈0.21. The h value is found highest for the sample BBC_1Zr_2, and it may be attributed to more number of delocalization of the 3d- electrons of Cr^{3+} ions. This is an act of the increased covalence nature of ligand bonds (Cr-O bonds) at higher concentration of ZrO_2 nanoparticles in the BBCZr glass ceramics [53]. Fig. 8 shows the Tanabe-Sugano diagram of Cr^{3+} ions (in d^3 configuration) in the BBC_1Zr_2 glass ceramic host. The $^4T_{2g}$ (F) and $^2T_{1g}$ (F) levels fall at $\frac{D_q}{B} = 2.3$ [54]. In weak crystal field $\frac{D_q}{B} < 2.3$ [5,27,54] and in strong fields $\frac{D_q}{B} > 2.3$ [8,46]. The ratio $\frac{D_q}{B}$ in the present samples is found to be in the range of 2.463–2.542 (as shown in Table 4), which confirms that the Cr^{3+} ions are presented in the strong ligand field of [CrO_6] octahedral sites [51].

3.3. Photoluminescence spectroscopy

3.3.1. Excitation spectrum

Fig. 9 shows the excitation spectrum of Cr^{3+} ions in the BBC_1Zr_1 glass ceramic sample monitored at $\lambda_{emission}$ = 694 nm. The spectrum has revealed two absorption bands due to the transitions $^4A_{2g}$(F) to $^4T_{1g}$(F) and $^4T_{2g}$(F) at 421 nm and 630 nm respectively. The intensity of the band attributed to $^4A_{2g}$(F) → $^4T_{1g}$(F) is found to be premier, and the excitation wavelength is confirmed as 421 nm [55,56]. Other samples have displayed same bands following the similar trend.

3.3.2. Emission spectra

Fig. 10 shows the emission spectra of Cr^{3+} ions in the present glass ceramic samples excited at $\lambda_{excitation}$ = 421 nm. The emission spectra of the samples have displayed two clear emission bands peaking at ≈550

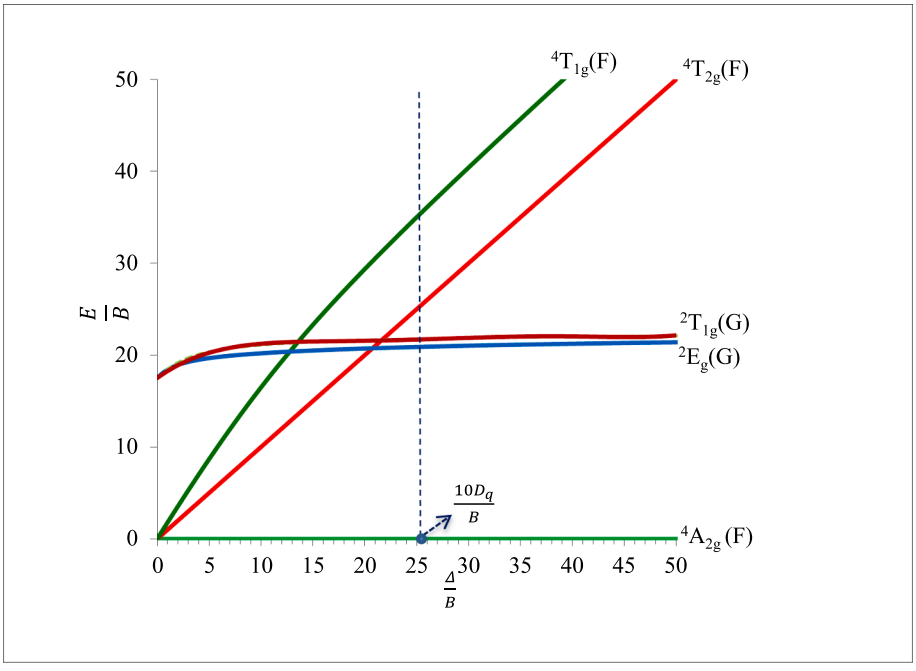

Fig. 8. Tanabe-Sugano diagram of Cr^{3+} ions (in d^3 configuration) in BBC_1Zr_2 glass ceramic.

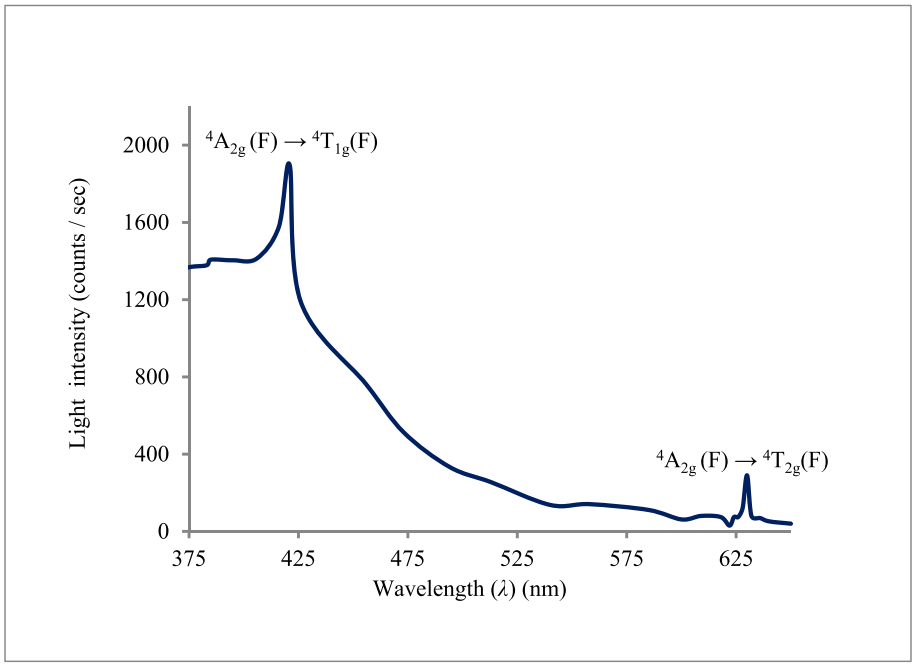

Fig. 9. Excitation spectrum of the BBC_1Zr_1 glass ceramic monitored for $\lambda_{emission}$ = 694 nm.

nm and ≈690 nm. The band in the green region (≈550 nm) is attributed to the spin-allowed transition $^4T_{2g}(F) \rightarrow {}^4A_{2g}(F)$ of Cr^{3+} ions [55,57]. And, the band discovered in red region (≈690 nm) is attributed to the spin-forbidden transition by $^2E_g(G) \rightarrow {}^4A_{2g}(F)$ of Cr^{3+} ions [55,57]. Table 5 shows the pertinent data on emission bands of these glass ceramics. Fig. 11 shows variation of intensity of green and red emission bands as a function of concentration of ZrO_2 nanoparticles in the host medium. The intensity of these emission bands is increased up to x = 1 mol % of ZrO_2 in the composition with redshift. Later, the intensity is decreased for x > 1 mol % of ZrO_2 with a slight blueshift. The change in intensity of emission bands may be occurred because of transformation of a chromium ions $Cr^{6+} \rightarrow Cr^{5+} \rightarrow Cr^{3+}$ ions with $[CrO_4]^{2-} \rightarrow [CrO_4]^{3-} \rightarrow$

Table 5
Pertinent data on emission bands of Cr^{3+} ions in the BBCZr glass ceramics.

Sample	$^4T_{2g}(F) \rightarrow {}^4A_{2g}(F)$ Green emission band (nm)	$^2E_g(G) \rightarrow {}^4A_{2g}(F)$ Red emission band (nm)
BBC_1Zr_0	551	690
$BBC_1Zr_{0.5}$	552	692
BBC_1Zr_1	556	696
$BBC_1Zr_{1.5}$	555	694
BBC_1Zr_2	553	693

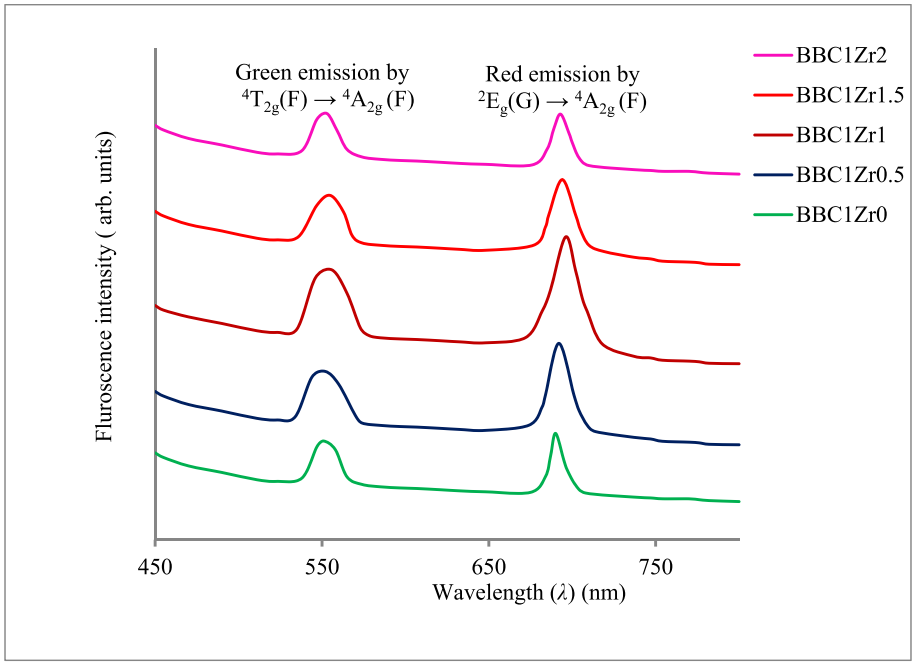

Fig. 10. Photoluminescence spectra of Cr^{3+} ions in BBCZr glass ceramics ($\lambda_{excitation}$ = 421 nm).

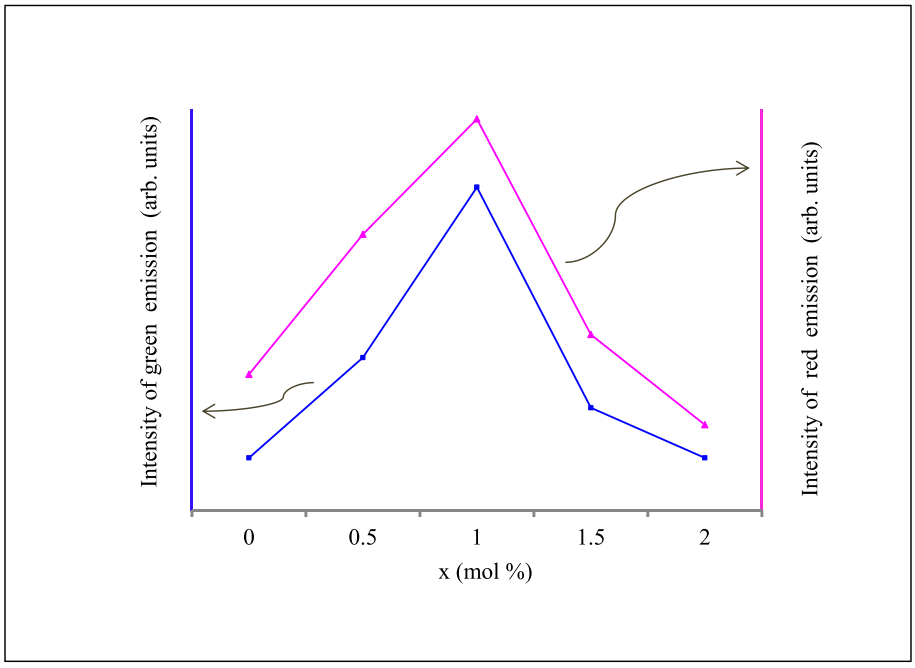

Fig. 11. Variation of intensity of green and red emission bands as a function of concentration of ZrO_2 nanoparticles.

$[CrO_6]$ units up to x = 1 mol %, and $Cr^{3+} \rightarrow Cr^{5+} \rightarrow Cr^{6+}$ ions with $[CrO_6] \rightarrow [CrO_4]^{3-} \rightarrow [CrO_4]^{2-}$ units for x > 1 mol %. Nevertheless, there could be non-radiative transitions of the $Cr^{5+}O^{-}$ and $Cr^{6+}O^{2-}$ centres thru deexcitations in the host medium; therefore the whole emission is primarily achieved by means of Cr^{3+} ions [58]. Here, we can notice a little broadening of the emission band of Cr^{3+} ions in the green region, which includes probably the charge transfer transition between the Bi^{3+} ion pairs at the B^{3+} cation of the borate host. Thus, we may say that the green band (≈550 nm) is observed to be broadened due to the overlapping of transitions $^4T_{2g}(F) \rightarrow {}^4A_{2g}(F)$ of Cr^{3+} ions with $^3P_1 \rightarrow {}^1S_0$ of Bi^{3+} ions [59]. Whereas, the red band (≈690 nm) of Cr^{3+} ions is relatively sharp, because of the strong crystal field associated with the Cr^{3+} ions [27]. Of course, another sharp spin forbidden transition $^2T_{1g}(G) \rightarrow {}^4A_{2g}(F)$ of Cr^{3+} ions may be merged with the dominant sharp transition $^2E_g(F) \rightarrow {}^4A_{2g}(G)$ of Cr^{3+} ions in the same region [27]. Therefore, these glass ceramics containing Zr^{4+} ions (in which the crystallization takes place simultaneously with increase of the ligand field around Cr^{3+} ions) are favorable hosts for the narrow transition of $^2E_g(F) \rightarrow {}^4A_{2g}(G)$ in the red region (≈690 nm). B^{3+} cations act as network modifiers that affect structural integrity of $[BO_4]$ units, modifying the energy levels of Cr^{3+} ions. Thus, Bi^{3+} ions and B^{3+} ions can enhance optical activity of Cr^{3+} ions, introducing the defect states (oxygen and charge defects) in the vicinity of $[CrO_6]$ octahedral sites. The Bi_2O_3-B_2O_3 glass ceramic host could facilitate prominent emission bands in visible region, making these materials valuable for applications in photonics and optical devices [27,58,59,60].

3.3.3. *Radiative transition characteristics*

The radiative transition characteristics of Cr^{3+} ions in the BBCZr glass ceramics have been carried out and the pertinent data is included in Table 6. The spontaneous emission transition probability (A) for a given emission band, total transition probability (A_T) of all the emission

Table 6
Radiative transition characteristics of Cr^{3+} ions in the BBCZr glass ceramics.

Sample	Refractive index (n_d)	Emission transition	Band position λ (nm)	Band width $d\lambda$ (nm)	Transition probability A (s^{-1})	Total transition probability A_T (s^{-1})	Branching ratio β_R%	Stimulated emission scattering cross-section σ^E x 10^{-21} (cm^2)	Radiative lifetime τ_R (μs)
BBC_1Zr_0	2.261	$^2E_g(G) \rightarrow {}^4A_{2g}(F)$	690	17	2842.82	8425.48	33.74	9.84	118.69
		$^4T_{2g}(F) \rightarrow {}^4A_{2g}(F)$	551	27	5582.66		66.26	4.95	
$BBC_1Zr_{0.5}$	2.265	$^2E_g(G) \rightarrow {}^4A_{2g}(F)$	692	20	2782.37	8264.13	33.67	8.26	121.01
		$^4T_{2g}(F) \rightarrow {}^4A_{2g}(F)$	552	32	5481.74		66.33	4.12	
BBC_1Zr_1	2.274	$^2E_g(G) \rightarrow {}^4A_{2g}(F)$	696	23	2685.74	7954.01	33.77	7.03	125.72
		$^4T_{2g}(F) \rightarrow {}^4A_{2g}(F)$	556	43	5268.27		66.23	3.01	
$BBC_1Zr_{1.5}$	2.271	$^2E_g(G) \rightarrow {}^4A_{2g}(F)$	694	17	2797.05	8265.94	33.84	9.82	120.98
		$^4T_{2g}(F) \rightarrow {}^4A_{2g}(F)$	555	40	5468.89		66.16	3.34	
BBC_1Zr_2	2.269	$^2E_g(G) \rightarrow {}^4A_{2g}(F)$	693	11	2877.99	8541.85	33.69	15.55	117.07
		$^4T_{2g}(F) \rightarrow {}^4A_{2g}(F)$	553	27	5663.87		66.31	5.06	

bands, branching ratio (β_R), stimulated emission scattering cross-section (σ^E), and radiative lifetime (τ_R) of Cr^{3+} ions can be determined using following known relations [29,61]:

$$A = \left(\frac{16\pi^3\nu^3}{3hc^3}\right)|\mu_d|^2 \quad (23)$$

$$A_T = \sum_{i=1}^{n} A \quad (24)$$

$$\beta_R = \frac{A}{A_T} \quad (25)$$

$$\tau_R = \frac{1}{A_T} \quad (26)$$

$$\sigma^E = \frac{A\lambda^4}{8\pi c n_d^2 \Delta\lambda} \quad (27)$$

Where, ν is frequency of the emission band, c is velocity of photon, μ_d denotes the dipole transition moment of the Cr^{3+} ions in present host, λ is the emission peak position, $\Delta\lambda$ is bandwidth, and n_d is refractive index of the sample. The value of branching ratio (β_R) of the transition $^4T_{2g}(F) \rightarrow {}^4A_{2g}(F)$ of Cr^{3+} ions is higher than that of the transition $^2E_g(G) \rightarrow {}^4A_{2g}(F)$ for all the samples. The transition $^4T_{2g}(F) \rightarrow {}^4A_{2g}(F)$ of Cr^{3+} ions in all the samples shows $\beta_R > 50$ %, confirming the highest possibility of emission of laser light in green color [29]. The value of τ_R of Cr^{3+} ions is observed to be the lowest for the sample BBC_1Zr_2 (at higher content of ZrO_2) which leads to greater non-radiative losses due to multi-phonon relaxations and causes poor quantum efficiency at higher content of ZrO_2 in the composition in the glass ceramics [62]. On the other hand, the value of τ_R of Cr^{3+} ions is observed to be the highest for the sample BBC_1Zr_1 (at x = 1 mol % of ZrO_2) which leads to lower non-radiative losses and yields good quantum efficiency for practical applications [29,62,63].

3.3.4. Correlation between surface roughness and photoluminescence

Increased RMS roughness (R_q) of the sample BBC_1Zr_1 (as shown in Table 1) enhances the effective scattering area of light emission, which can lead to energy shift for excitons or phonons. As a result, inhomogeneous broadening of the emission peaks occurs. Consequently, the increase in line broadening of emission peaks could decrease the stimulated emission cross-section (σ^E) (as shown in Table 6). Thus, the sample BBC_1Zr_1 has exhibited the lowest value of the stimulated emission cross section (σ^E) due to the higher values of effective bandwidth ($\Delta\lambda$) of the emission bands as observed in photoluminescence spectrum of that sample (Fig. 10). Similar studies on emission bands of Sm^{3+} ions were carried out by R.N.A. Prasad et al [63].

Fig. 12 shows the variation of relative intensity of red emission band (I/I_{max}) and RMS roughness (R_q) as a function of concentration of ZrO_2 in the BBCZr glass ceramics. It is very clear from the figure that the relative intensity of the red emission band and rms roughness are highest at x = 1 mol % of ZrO_2 in the composition. Thus, we note that the intensities of emission bands are very reliant on the surface profile that can be determined by the crystallinity and grain size of the glass ceramics [64,65].

3.3.5. Energy level diagram

Fig. 13 (a) illustrates the energy level diagram (excitation and emission schemes) of Cr^{3+} ions in presence of octahedral field with d^3 configuration of one of the samples (i.e., BBC_1Zr_2 glass ceramic). As per the Tanabe–Sugano diagram, the position of excited states ($^4T_{2g}(F)$ and $^2E_g(G)$ states) can be altered subject to the field strength in the d^3-configuration of Cr^{3+} ions in $[CrO_6]$ site. The ratio of ligand field parameters ($\frac{D_q}{B}$) can determine exact positions of excited states $^4T_{2g}(F)$ and $^2E_g(G)$ relatively [51]. If $\frac{D_q}{B} > 2.3$, Cr^{3+} ions present in high field sites and the energy of $^2E_g(G)$ state is less than $^4T_{2g}(F)$ state, which yields two narrow emission lines $^2E_g(G) \rightarrow {}^4A_{2g}(F)$ (R_1-line) and $^2T_{1g}(G) \rightarrow {}^4A_{2g}(F)$ (R_2-line) spin-forbidden transitions in the hosts like crystals, nanophosphors, glass ceramics, etc [8,46]. Conversely, if $\frac{D_q}{B} < 2.3$, Cr^{3+} ions present in low field sites and the energy of $^2E_g(G)$ state is greater than $^4T_{2g}(F)$ state, generating a broad emission band by $^4T_{2g} \rightarrow {}^4A_{2g}(F)$ spin-allowed transition in the amorphous hosts like glasses [5,27,54,58]. In case of the present BBCZr glass ceramic samples, the higher electronegativity of bismuth ions (Bi^{3+} ions) create an environment in which Cr^{3+} ions have limited interaction with the NBOs and electronic charge defects of O^{2-} (as these defects are slightly attracted towards the nearby Bi^{3+} ions), resulting in small amount of localized electrons around the

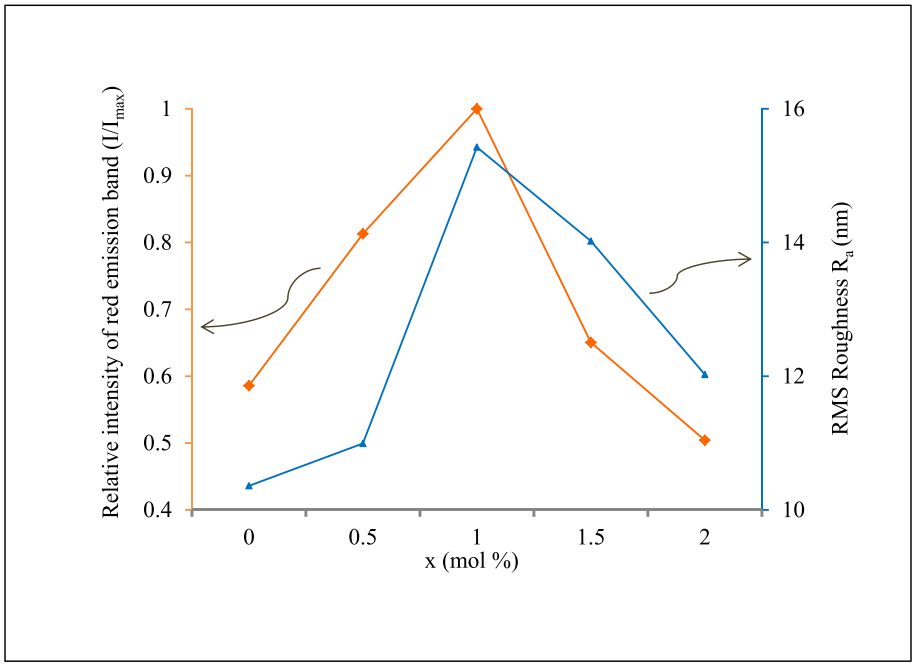

Fig. 12. Variation of relative intensity of red emission band (I/I_{max}) and RMS roughness (R_q) as a function of concentration of ZrO_2 in the BBCZr glass ceramics.

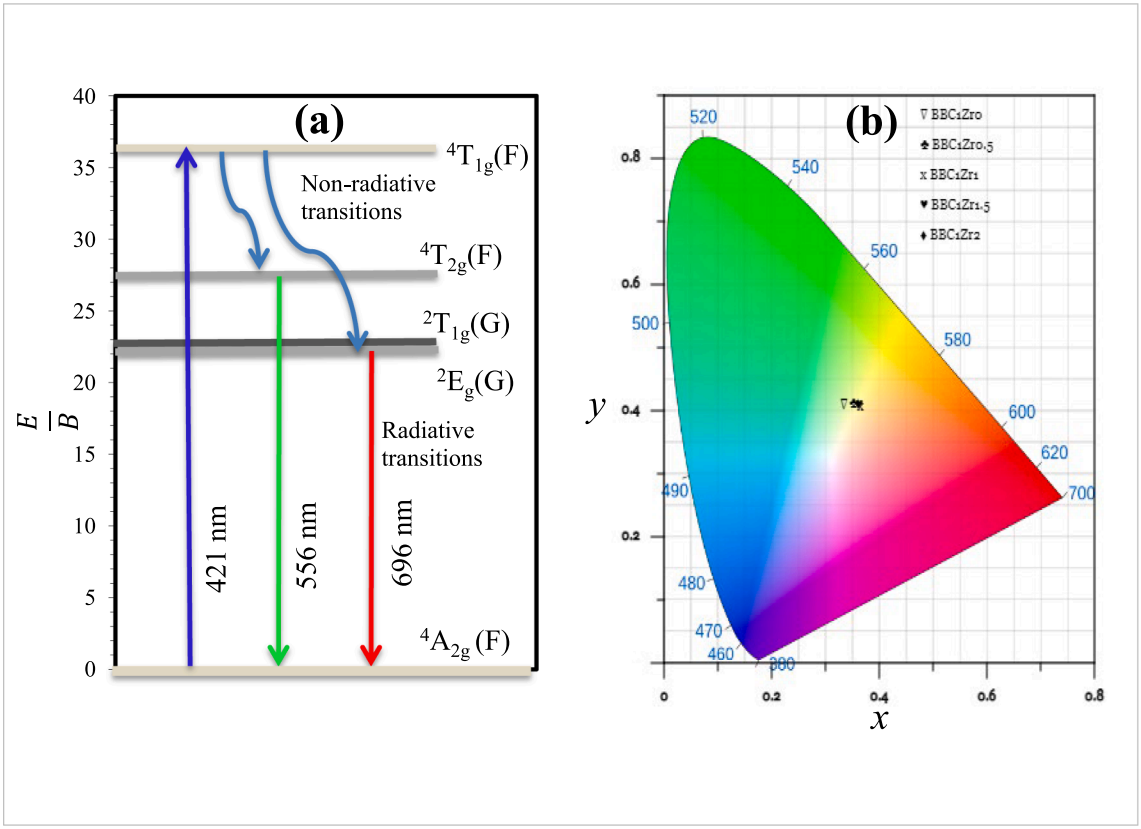

Fig. 13. (a) Energy level diagram of Cr^{3+} ion in BBC_1Zr_1 glass ceramic host. (b) CIE chromaticity diagram of BBCZr glass ceramics doped with 1 mol % of Cr_2O_3.

Cr^{3+} ions. So that, lower the ionic nature of Cr-O bonding of $[CrO_6]$ octahedron yields lower value of Racah parameter B [66]. Consequently, the ratio is determined as $\frac{D_q}{B} > 2.3$ for all the samples, hence the Cr^{3+} ions would be placed in high ligand field, thereby the energy level of $^2E_g(G)$ state is shifted down than that of $^4T_{2g}(F)$ state. Thus, the Cr^{3+} ions have produced two emission bands $^2T_{2g}(F) \rightarrow {}^4A_{2g}(F)$ (green emission) and $^2E_g(G) \rightarrow {}^4A_{2g}(F)$ (red emission) based on local coordination of Cr^{3+} ions in the high-field sites of their crystal lattice [27,55,57,58,66].

3.3.6. *CIE diagram*

The CIE chromaticity diagram 1931 of BBCZr glass ceramics is presented in Fig. 13 (b). It depicts CIE co-ordinates (*x, y*) and correlated color temperature (*CCT*) for possible production of visible light sources as recorded in Table 7. The values of (*x, y*) and *CCT* have been estimated by the software tool developed by E.H.H. Hasabeldaim et al [67]. The determined values of (*x, y*) and *CCT* for the BBCZr glass ceramics have been shifted towards high wavelength region following the path of green-yellow-orange as observed in Fig. 13 (b). These glass ceramics may act as active laser media or LED sources, particularly for tunable solid state lasers and LEDs in the visible band based on local coordination of Cr^{3+} ions in the high-field sites of their crystal lattice [2,4,27,55,56,57,58,66]. The appropriate concentration of dopant zirconium ions (Zr^{4+} ions) are used to facilitate a precise structural medications around the active Cr^{3+} ions in BBCZr glass ceramics, there by excitation and emission schemes can be tailor made. Thus, these glass ceramics may be used for developing the fluorescent multi-color display systems [68].

Table 7
CIE coordinates *(x, y)* and respective *CCT* temperature of Cr^{3+} ions in BBCZr glass ceramics.

Sample	CIE co-ordinates		*CCT*(K)
	x	*y*	
BBC_1Zr_0	0.334	0.409	5464.14
$BBC_1Zr_{0.5}$	0.351	0.411	4973.40
BBC_1Zr_1	0.366	0.407	4534.77
$BBC_1Zr_{1.5}$	0.363	0.408	4616.22
BBC_1Zr_2	0.361	0.411	4686.22

4. Conclusion

The AFM images confirmed the heterogeneous ceramic nature of BBCZr glass ceramics. The values of average roughness (R_a) of the samples were observed in the range of 7.714–10.763 nm with the average value of 8.903 nm. The values of rms roughness (R_q) of the samples were observed in the range of 9.991–15.426 nm with the average value of 12.136 nm. The sample BBC_1Zr_1 showed the highest values of R_a and R_q, showing surfaces that are rougher than those of other samples. The surface skew ness (R_{sk}) value of the BBCZr glass ceramics was found to be negative, demonstrating the presence of more number of peaks than troughs (more crystal growth) after the heat treatment. The values of Kurtosis coefficient (R_{ku}) have been obtained in the range of 1.526–6.232 with the average 3.540, indicating presence of highly concentrated sharp peaks around the mean value. The optical absorption spectra confirmed the presence of chromium ions in three stable valence states such as Cr^{3+}, Cr^{5+}, and Cr^{6+} states. The values of optical bandgap (E_o) and Urbach energy (E_u) of the samples obtained from the three methods viz., Tauc, ASF, and DASF were constituent. The DASF method was found to be more advantageous than the remaining two methods, because this method did not include the nature of transition (in terms of *m*), thickness of the sample (*d*), and the effect of charge transfer transitions in the UV region. The crystal field parameter (D_q), Racah parameters (*B & C*), and Nephelauxetic parameter (*h*) confirmed the presence of Cr^{3+} ions in strong crystal field (as $\frac{D_q}{B} > 2.3$). The value of *h* was estimated as ≈1.4 for the present samples. The value

of *h* was observed to be highest for the sample BBC_1Zr_2, which could be an act of the increased covalence nature of ligand bonds (Cr-O bonds) at higher content of ZrO_2 nanoparticles (x = 2 mol %) in the composition of the BBCZr glass ceramics. The emission spectra displayed two clear emission bands peaking at ≈550 nm and 690 nm. The band in the green-region (≈550 nm) was attributed by a spin-allowed transition $^4T_{2g}(F) \rightarrow {}^4A_{2g}(F)$ of Cr^{3+} ions. And, the band observed in red region (≈690 nm) was attributed by a spin-forbidden transition by $^2E_g(G) \rightarrow {}^4A_{2g}(F)$ of Cr^{3+} ions. The values of (*x, y*) coordinates and *CCT* in the CIE diagram were shifted from green to orange region as the content of ZrO_2 nanoparticles increased gradually. In this way, the BBCZr glass ceramics will be useful for developing the tunable solid-state lasers and LEDs in the visible band based on local coordination of Cr^{3+} ions in the crystal lattice. The radiative lifetime (τ_R) of Cr^{3+} ions is observed to be the highest for the sample BBC_1Zr_1 (at x = 1 mol % of ZrO_2) which results in reduced non-radiative losses and yields good quantum efficiency for practical applications.

CRediT authorship contribution statement

Adepu Navalika: Writing – review & editing, Writing – original draft, Software, Resources, Methodology, Investigation, Formal analysis, Data curation, Conceptualization. **Linganaboina Srinivasa Rao:** Writing – review & editing, Writing – original draft, Visualization, Validation, Supervision, Software, Resources, Project administration, Methodology, Investigation, Funding acquisition, Formal analysis, Data curation, Conceptualization. **Tumu Venkatappa Rao:** Writing – review & editing, Writing – original draft, Visualization, Validation, Supervision, Software, Resources, Methodology, Investigation, Formal analysis, Data curation, Conceptualization. **Shamima Hussain:** Writing – review & editing, Validation, Resources, Funding acquisition, Formal analysis, Data curation. **Sujay Chakravarty:** Writing – review & editing, Validation, Resources, Formal analysis, Data curation.

Declaration of competing interest

The authors declare that they have no known competing financial interests or personal relationships that could have appeared to influence the work reported in this paper.

Acknowledgement

The authors (Dr. L. Srinivasa Rao and Dr. S. Hussain) acknowledge the financial support from UGC-DAE CSR through a Collaborative Research Scheme (CRS) project number CRS/2021-22/04/615. One of the authors (A. Navalika) thanks UGC DAE CSR for awarding Junior Research Fellowship (JRF). The authors acknowledge the research facilities provided by VNRVJIET Hyderabad, UGC-DAE CSR Kalpakam, and NIT Warangal. The authors thank Editorial office, Journal of Alloys Compounds for facilitating the 'Article Transfer Service' for this research paper.

Data availability

No data was used for the research described in the article.

References

[1] M. He, J. Jia, J. Zhao, X. Qiao, J. Du, X. Fan, Glass-ceramic phosphors for solid state lighting: a review, Ceram. Int. 47 (2021) 2963–2980, https://doi.org/10.1016/j.ceramint.2020.09.227.

[2] L. Ouachouo, M. Jerroudi, A. Ouaha, H. Es-soufi, S. Taoussi, I. Chaiboub, E. Haily, B. Manoun, L. Bih, Electrical, optical, and structural studies of lithium tungstate-based-phosphate glasses and glass-ceramics, Mater. Sci. Eng., B 308 (2024) 117591, https://doi.org/10.1016/j.mseb.2024.117591.

[3] Z. Guo, L. Wang, J. Huimin Lv, H. Shao, S. Zhang, T. Wang, C.S. Wang, Preparation and luminescence properties of Tb^{3+} doped and Tb^{3+}/Sm^{3+} co-doped $Na_3Y(PO_4)_2$ crystalline glass ceramics, Mater. Sci. Eng., B 272 (2021) 115352, https://doi.org/10.1016/j.mseb.2021.115352.

[4] W. Liu, Z. Xiao, L. Li, Z. Wen, X. Xu, S. Qin, J. Huang, W. You, L. Han, J. Yu, Selective enrichment strategy induces ultra-broadband NIR emission in Cr^{3+}-doped multi-phase glass-ceramics for NIR spectroscopy applications, Ceram. Int. 49 (2023) 38318–38330, https://doi.org/10.1016/j.ceramint.2023.09.164.

[5] H. Liang, Z. Luo, K. Wu, J. Tong, C. Wen, P. Zhang, S. Liu, Z. Zhou, A. Lu, Structure and tunable broadband near-infrared luminescence of Cr^{3+} in borophosphate glass, Ceram. Int. 48 (2022) 34617–34626, https://doi.org/10.1016/j.ceramint.2022.08.049.

[6] G. Murali Krishna, B. Anila Kumari, M. Srinivasa Reddy, N. Veeraiah, Characterization and physical properties of Li_2O–CaF_2–P_2O_5 glass ceramics with Cr_2O_3 as a nucleating agent—Physical properties, J. Solid. State. Chem. 180 (2007) 2747–2755, https://doi.org/10.1016/j.jssc.2007.07.025.

[7] Z. Zhang, K.T.V. Grattan, A.W. Palmer, Temperature dependences of fluorescence lifetimes in Cr^{3+}-doped insulating crystals, Phys. Rev. B 48 (1993) 7772–7778, https://doi.org/10.1103/PhysRevB.48.7772.

[8] W. Dai, F. Chi, B. Lou, X. Wei, J. Cheng, S. Liu, M. Yin, Temperature-dependent luminescent properties of Cr^{3+} doped $ZnGa_2O_4$ far-red emitting phosphor, Opt. Mater. 116 (2021) 111104, https://doi.org/10.1016/j.optmat.2021.111104.

[9] L. Srinivasa Rao, S. Hussain, A. Navalika, B. Chennakesava Rao , T. Venkatappa Rao, F.C. Hila, Effect of ZnO nanoparticles on physical, optical and radiation shielding properties of Bi_2O_3-B_2O_3-Cr_2O_3 glasses, Results in Optics 12 (2023) 100491, doi: 10.1016/j.rio.2023.100491.

[10] L. Srinivasa Rao, S. Hussain, A.Navalika, K. Aruna Prabha, N.V. Suresh Kumar, B. Chennakesava Rao Effect of ZnO nanoparticles on structure and magnetic properties of Bi_2O_3-B_2O_3: Cr_2O_3 glasses, Mater. Today: Proc. 92 (2) (2023) 886-891, doi: 10.1016/j.matpr.2023.04.480.

[11] L. Srinivasa Rao, A. Navalika, S. Hussain, T. Venkatappa Rao, Structural evolution of versatile Bi_2O_3-B_2O_3-Cr_2O_3: ZrO_2 glass ceramics monitored by Raman and EPR spectroscopy, J. Mol. Struct. 1301 (2024) 137458, doi: 10.1016/j.molstruc.2023.137458.

[12] L. Srinivasa Rao, S. Hussain, A. Navalika, F.C. Hila, Morphology, structural, and radiation shielding characteristics of Bi_2O_3-B_2O_3-Cr_2O_3: ZrO_2 glass ceramics, Ceram. Int. 50 (6) (2024) 9811-9819, doi: 10.1016/j.ceramint.2023.12.302.

[13] S. Liu, M. Liu, S. Jiang, C. Li, Y. Zeng, Y. Huang, D. Zhou, Fabrication of SiO_2-doped $Ba_{0.85}Sr_{0.15}TiO_3$ glass–ceramic films and the measurement of their pyroelectric coefficient, Mater. Sci. Eng., B 99 (1–3) (2003) 511-515, doi: 10.1016/S0921-5107(02)00516-0.

[14] Wei-che Chang, Shih-chin Lee, Chih-hao Yang,Tien-chai Lin, Opto-electronic properties of chromium doped indium–tin-oxide films deposited at room temperature, Mater. Sci. Eng., B 153 (1–3) (2008) 57-61, doi: 10.1016/j.mseb.2008.09.046.

[15] F. Abdi, Investigation of the porosity and particle size effects on the optical constants of Mn star shape thin films, Phys. b: Condens. Matter. 677 (2024) 415691, https://doi.org/10.1016/j.physb.2024.415691.

[16] F. Juhim, F.P. Chee, A. Awang, P.Y. Moh, K.A. Mohd Salleh, S. Ibrahim, J. Dayou, A. Alalawi, M.S. Al-Buriahi, Study of gamma radiation shielding on tellurite glass containing TiO_2 and Al_2O_3 nanoparticles, Heliyon 9 (2023)-22529, doi: 10.1016/j.heliyon.2023.e22529.

[17] Z. Lou, Y. Zhang, Y. Li, L. Xu, Study on microscopic physical and chemical properties of biomass materials by AFM, J. Mater. Res. Technol. 24 (2023) 10005–10026, https://doi.org/10.1016/j.jmrt.2023.05.176.

[18] L. Auvray, H. Dumont, J. Dazord, Y. Monteil, J. Bouix, C. Bru-Chevallier, L. Grenouillet, MOVPE growth of GaAsN: surface study by AFM and optical properties, Mater. Sci. Semicond. Process 3 (2000) 505–509, https://doi.org/10.1016/S1369-8001(00)00095-0.

[19] E. Kulpina, A.N. Babkina, K. Zyryanova, A. Bukhvostov, N. V. Platonova, Chromium-doped borate glass ceramics for optical temperature sensors, Optical Sensors (2021), SPIE 2021: p. 49, doi: 10.1117/12.2589152.

[20] S. Ahmadi, B.E. Yekta, H. Sarpoolaky, A. Aghaei, Preparation of monolithic transparent mullite-based glass-ceramics by the sol–gel method, J. Non. Cryst. Solids 575 (2022) 121186, https://doi.org/10.1016/j.jnoncrysol.2021.121186.

[21] D. Nečas, P. Klapetek, Gwyddion: an open-source software for SPM data analysis, Open Physics 10 (2012), https://doi.org/10.2478/s11534-011-0096-2.

[22] S. Zhao, Y. Li, Y. Wang, Z. Ma, X. Huang, Quantitative study on coal and shale pore structure and surface roughness based on atomic force microscopy and image processing, Fuel 244 (2019) 78–90, https://doi.org/10.1016/j.fuel.2019.02.001.

[23] L. Srinivasa Rao, T. Venkatappa Rao, Sd. Naheed, P. Venkateswara Rao, Structural and optical properties of zinc magnesium oxide nanoparticles synthesized by chemical co-precipitation, Mater. Chem. Phys. 203 (2018) 133–140, https://doi.org/10.1016/j.matchemphys.2017.09.048.

[24] J. Tauc, A. Menth, States in the gap, J. Non Cryst. Solids 8–10 (1972) 569–585, https://doi.org/10.1016/0022-3093(72)90194-9.

[25] D. Souri, K. Shomalian, Band gap determination by absorption spectrum fitting method (ASF) and structural properties of different compositions of $(60–x)V_2O_5$-$40TeO_2$-xSb_2O_3 glasses, J. Non Cryst. Solids 355 (2009) 1597–1601, https://doi.org/10.1016/j.jnoncrysol.2009.06.003.

[26] D. Souri, Z.E. Tahan, A new method for the determination of optical band gap and the nature of optical transitions in semiconductors, Appl. Phys. B 119 (2015) 273–279, https://doi.org/10.1007/s00340-015-6053-9.

[27] B.V. Padlyak, W. Ryba-Romanowski, R. Lisiecki, V.T. Adamiv, Y.V. Burak, I. M. Teslyuk, Synthesis, EPR and optical spectroscopy of the Cr-doped tetraborate glasses, Opt. Mater. 34 (12) (2012) 2112–2119, https://doi.org/10.1016/j.optmat.2012.06.014.

[28] C.R. Kesavulu, R.P.S. Chakradhar, C.K. Jayasankar, J.L. Rao, EPR, optical, photoluminescence studies of Cr^{3+} ions in Li_2O–Cs_2O–B_2O_3 glasses – An evidence of mixed alkali effect, J. Mol. Struct. 975 (2010) 93–99, https://doi.org/10.1016/j.molstruc.2010.03.091.

[29] L. Srinivasa Rao, M. Srinivasa Reddy, M.V. Ramana Reddy, N. Veeraiah, Spectroscopic features of Pr^{3+}, Nd^{3+}, Sm^{3+} and Er^{3+} ions in Li_2O–MO (Nb_2O_5, MoO_3 and WO_3)–B_2O_3 glass systems, Physica B Condens. Matter 403 (2008) 2542–2556, https://doi.org/10.1016/j.physb.2008.01.043.

[30] H. Li, J. Cao, J. Lu, B. Lin, Y. Lu, S. Shi, W. Yang, Y. Hong, T. Liu, M. Liu, Effect of microwave-assisted cyclic oxidation on the coal internal and surface structure based on NMR and AFM, Energy 288 (2024) 129872, https://doi.org/10.1016/j.energy.2023.129872.

[31] V.L. Mironov, O.G. Udalov, B.A. Gribkov, A.A. Fraerman, Comparative X-ray reflectometry and atomic force microscopy of surfaces with non-Gaussian roughness, J. Appl. Phys. 104 (2008), https://doi.org/10.1063/1.2977753.

[32] A.Z. Juri, X.-F. Song, Y. Nakanishi, J. Dudley, L. Jamieson, L. Yin, Surface fractures in pre-crystallized and crystallized zirconia-containing lithium silicate glass-ceramics generated in ultrasonic vibration-assisted machining, J. Mech. Behav. Biomed. Mater. 147 (2023) 106132, https://doi.org/10.1016/j.jmbbm.2023.106132.

[33] M. Srinivasa Reddy, S.V.G.V.A. Prasad, N. Veeraiah, Valence and coordination of chromium ions in ZnO–Sb_2O_3–B_2O_3 glass system by means of spectroscopic dielectric relaxation studies, Phys. Status Solidi A 204 (2007) 816–832, https://doi.org/10.1002/pssa.200622250.

[34] M.A. Hassan, F. Ahmad, Z.M. Abd El-Fattah, Novel identification of ultraviolet/visible Cr^{6+}/Cr^{3+} optical transitions in borate glasses, J Alloys Compd. 750 (2018) 320–327, https://doi.org/10.1016/j.jallcom.2018.03.351.

[35] H.Y. Morshidy, A.R. Mohamed, A.A. Abul-Magd, M.A. Hassan, Role of high energy Cr^{6+} optical transition induced by rare earth ion (La^{3+}) in compositional-dependent borate glass, Mater. Chem. Phys. 289 (2022) 126503, https://doi.org/10.1016/j.matchemphys.2022.126503.

[36] M.A. Marzouk, F.H. ElBatal, K.M. ElBadry, H.A. ElBatal, Optical, structural and thermal properties of sodium metaphosphate glasses containing Bi_2O_3 with interactions of gamma rays, Spectrochim. Acta, Part A 171 (2017) 454–460, https://doi.org/10.1016/j.saa.2016.08.038.

[37] H.A. El Batal, F.H. El Batal, M.A. Azooz, M.A. Marzouk, A.A. El Kheshen, N. A. Ghoneim, F.M. Ezz El Din, A.M. Abdelghany, Comparative shielding behavior of binary PbO–B_2O_3 and Bi_2O_3–B_2O_3 glasses with high heavy metal oxide contents towards gamma irradiation revealed by collective optical, FTIR and ESR measurements, J. Non-Cryst. Solids 572 (2021) 121090, https://doi.org/10.1016/j.jnoncrysol.2021.121090.

[38] L. Srinivasa Rao, F.C. Hila, M. Srinivasa Reddy, S. Hussain, Effect of zirconium oxide nanoparticles on thermal, optical, and radiation shielding properties of Bi_2O_3-B_2O_3-MnO_2 glasses, Appl. Radiat. Isot. 205 (2024) 111183, https://doi.org/10.1016/j.apradiso.2024.111183.

[39] M.D. Hanwell, D.E. Curtis, D.C. Lonie, T. Vandermeersch, E. Zurek, G.R. Hutchison, Avogadro: an advanced semantic chemical editor, visualization, and analysis platform, J. Cheminform 4 (2012) 17, https://doi.org/10.1186/1758-2946-4-17.

[40] G. Cruciani, M. Dondi, M. Ardit, T.S. Lyubenova, J.B. Carda, F. Matteucci, A. L. Costa, Malayaite ceramic pigments: A combined optical spectroscopy and neutron/X-ray diffraction study, Mater. Res. Bull. 44 (8) (2009) 1778–1785, https://doi.org/10.1016/j.materresbull.2009.03.006.

[41] M.A. Algradee, Y.H. Elbashar, A.B. Alwany, H.H. Hassan, R. El-Mallawany, Impact of Yb_2O_3 on the physical, bonding, dispersion and dielectric properties of Li_2O–ZnO–P_2O_5 glasses, Mater. Sci. Semicond. Process. 140 (2022) 106362, https://doi.org/10.1016/j.mssp.2021.106362.

[42] L. Srinivasa Rao, V. Ravi Kumar, P. Naresh, P. Venkateswara Rao, N. Veeraiah, Optical absorption and photoluminescence properties of vanadium ions in 'lithium-tungsten-borate' oxide glasses, Mater. Today: Proc. 5 (2018) 26290–26297, https://doi.org/10.1016/j.matpr.2018.08.079.

[43] P.W. Anderson, Absence of diffusion in certain random lattices, Phys. Rev. 109 (1958) 1492–1505, https://doi.org/10.1103/PhysRev.109.1492.

[44] E. Cervantes-Juárez, A.N. Meza-Rocha, S. Carmona-Téllez, M. Palomino-Ovando, O. Zelaya-Angel, M.E. Zayas, O. Soriano-Romero, U. Salazar-Kuri, R. Lozada-Morales, Burstein Moss effect in CdO–V_2O_5–P_2O: Er^{3+} glasses, and the Yb^{3+} concentration effect on up conversion and downshifting emissions, J. Alloys Compd. 834 (2020) 154966, https://doi.org/10.1016/j.jallcom.2020.154966.

[45] Y. Tanabe, S. Sugano, On the Absorption Spectra of Complex Ions. I, J. Physical Soc. Japan 9 (1954) 753–766, https://doi.org/10.1143/JPSJ.9.753.

[46] V. Singh, R.P.S. Chakradhar, J.L. Rao, S.H. Kim, EPR and luminescence studies of Cr^{3+} doped $MgSrAl_{10}O_{17}$ phosphor synthesized by a low-temperature solution combustion route, J. Lumin. 154 (2014) 328–333, https://doi.org/10.1016/j.jlumin.2014.03.035.

[47] F. Rasheed, K.P. O'Donnell, B. Henderson, D.B. Hollis, Disorder and the optical spectroscopy of Cr^{3+} -doped glasses. II. Glasses with high and low ligand fields, J. Phys.: Condens. Matter 3 (1991) 3825–3840, https://doi.org/10.1088/0953-8984/3/21/015.

[48] M. Casalboni, V. Ciafardone, G. Giuli, B. Izzi, E. Paris, P. Prosposito, An optical study of silicate glass containing Cr^{3+} and Cr^{6+} ions, J. Phys.: Condens. Matter 8 (1996) 9059–9069, https://doi.org/10.1088/0953-8984/8/46/011.

[49] J.W. Orton, Electron paramagnetic resonance: an introduction to transition group ions in crystals, Iliffe Books Ltd., London, 1968.

[50] B. Henderson, G. Frank Imbusch, Optical Spectroscopy of Inorganic Solids,Volume 44, Monographs on the physics and chemistry of materials, Oxford science publications, (2006).

[51] C.R. Kesavulu, R.P.S. Chakradhar, R.S. Muralidhara, J.L. Rao, R.V. Anavekar, EPR, optical absorption and photoluminescence properties of Cr^{3+} ions in lithium borophosphate glasses, J. Alloys Compd. 496 (2010) 75–80, https://doi.org/10.1016/j.jallcom.2010.02.119.

[52] S. Adachi, Practical consideration on Racah parameter and Tanabe−Sugano diagram analyses for Mn^{4+} and Cr^{3+}-activated phosphors, J. Lumin. 273 (2024) 120628, https://doi.org/10.1016/j.jlumin.2024.120628.

[53] W. Seeber, D. Ehrt, H. Ebendorff-Heidepriem, Spectroscopic and laser properties of Ce^{3+} Cr^{3+} Nd^{3+} co-doped fluoride phosphate and phosphate glasses, J. Non Cryst. Solids 171 (1994) 94–104, https://doi.org/10.1016/0022-3093(94)90036-1.

[54] X. Long, Z. Lin, Z. Hu, G. Wang, T.P.J. Han, Optical study of Cr^{3+}-doped $LaSc_3(BO_3)_4$ crystal, J. Alloys. Compd. 347 (2002) 52–55, https://doi.org/10.1016/S0925-8388(02)00785-5.

[55] K.M. Girish, B.S. Goud, R. Naik, S.C. Prashantha, H. Nagabhushana, R. Lavanya, G. V. Ashok Reddy, J.H. Kim, Photoluminescence and photocatalytic properties of Zn_2TiO_4: C^{r3} + nanophosphors, Inorg. Chem. Commun. 151 (2023) 110628, https://doi.org/10.1016/j.inoche.2023.110628.

[56] R. Zhang, Y. Zhang, J. Ding, W. Wan, W. Zhu, G. Deng, W. Chen, M. Zhong, Z. Chen, Z. Ma, X. Liu, J. Qiu, Effect of ZrO_2 and TiO_2 on the micro-structure and NIR luminescence of mullite type Cr:$Al_4B_2O_9$ glass ceramics, J. Eur. Ceram. Soc. 44 (4) (2024) 2437–2444, https://doi.org/10.1016/j.jeurceramsoc.2023.11.041.

[57] I. Kashif, A. Ratep, Blue, Red, and Green Emission from Chromium and Copper Metal Doped Lithium Borate Glass, IOP Conf. Ser.: Mater. Sci. Eng. 956 (2020) 012013, doi: 10.1088/1757-899X/956/1/012013.

[58] A.M. Othman, Z.M. Abd El-Fattah, M. Farouk, A.M. Moneep, M.A. Hassan, Optical spectroscopy of chromium doped bismuth-lithium borate glasses, J. Non Cryst. Solids 558 (2021) 120665, https://doi.org/10.1016/j.jnoncrysol.2021.120665.

[59] H.C. Swart, R.E. Kroon, Ultraviolet and visible luminescence from bismuth doped materials, Opt. Mater.: X 2 (2019) 100025, doi: 10.1016/j.omx.2019.100025.

[60] G. Ravi Kumar, M.C. Rao, Structural and photoluminescence investigations of Cr^{3+} mixed Li_2O—Bi_2O_3—ZrO_2—SiO_2 glass ceramics for optoelectronic device application, Optik 181 (2019) 721–731, https://doi.org/10.1016/j.ijleo.2018.12.110.

[61] W.P. Healy, Book chapter- Electrodynamics, Quantum, in: In a Book- Encyclopedia of Physical Science and Technology (third Edition), Academic Press, 2003, pp. 199–217, https://doi.org/10.1016/B0-12-227410-5/00207-6.

[62] J. Tong, Z. Luo, X. Liu, P. He, H. Liang, A. Lu, Effects of Cr^{3+} content on the structure and fluorescence properties of SiO_2–Na_2O–Y_2O_3–P_2O_5 glasses and glass-ceramics with $Na_3YSi_2O_7$ crystal phase, J. Non-Cryst. Solids 619 (2023) 122551, https://doi.org/10.1016/j.jnoncrysol.2023.122551.

[63] R.N.A. Prasad, L. Srinivasa Rao, T. Anil Babu, K. Neeraja, N. Krishna Mohan, Structural and photoluminescence characteristics of PbO-M_2O_3(M_2O_3 = Al_2O_3, Sb_2O_3 and Bi_2O_3)-WO_3-B_2O_3: Sm_2O_3 glasses suitable for orange-red lasers, Optik 244 167563 (2021), https://doi.org/10.1016/j.ijleo.2021.167563.

[64] K.S. Shim, H.K. Yang, B.K. Moon, B.C. Choi, J.H. Jeong, J.S. Bae, K.H. Kim, Crystallinity and surface roughness dependent photoluminescence of $Y_{1-x}Gd_xVO_4$: Eu^{3+} thin films grown on Si (100) substrate, Thin Solid Films 517 (17) (2009) 5137–5140, https://doi.org/10.1016/j.tsf.2009.03.005.

[65] A. Wagner, B. Ratzker, S. Kalabukhov, N. Frage, Enhanced external luminescence quantum efficiency of ceramic phosphors by surface roughening, J. Lumine. 213 (2019) 454–458, https://doi.org/10.1016/j.jlumin.2019.05.058.

[66] F.S. De Vicente, F.A. Santos, B.S. Simões, S.T. Dias, M. Siu Li, EPR, optical absorption and luminescence studies of Cr^{3+}-doped antimony phosphate glasses, Opt. Mater. (amst) 38 (2014) 119–125, https://doi.org/10.1016/j.optmat.2014.10.012.

[67] E.H.H. Hasabeldaim, H.C. Swart, R.E. Kroon, Luminescence and stability of Tb doped CaF_2 nanoparticles, RSC Adv. 13 (2023) 5353–5366, https://doi.org/10.1039/D2RA07897J.

[68] P. Zhang, Z. Luo, X. Liu, P. He, S. Liu, W. Lei, H. Liang, Z. Zhou, A. Lu, Effects of coordination field environment on the fluorescence properties of transparent $ZnGa_2O_4$ glass-ceramics doped with Mn^{2+} and Cr^{3+} ions, J. Alloys Compd. 926 (2022) 166844, https://doi.org/10.1016/j.jallcom.2022.166844.